

Quantum rates in dissipative systems with spatially varying friction

Oliver Bridge ¹, Paolo Lazzaroni,² Rocco Martinazzo ³,
Mariana Rossi ², Stuart C. Althorpe,¹ and Yair Litman ^{1,*}

¹*Yusuf Hamied Department of Chemistry, University of Cambridge, Lensfield Road, Cambridge, CB2 1EW, UK*

²*MPI for the Structure and Dynamics of Matter, Luruper Chaussee 149, 22761 Hamburg, Germany*

³*Department of Chemistry, Università degli Studi di Milano, Via Golgi 19, 20133 Milano, Italy*

We investigate whether making the friction spatially dependent on the reaction coordinate introduces quantum effects into the thermal reaction rates for dissipative reactions. Quantum rates are calculated using the numerically exact multi-configuration time-dependent Hartree (MCTDH) method, as well as the approximate ring-polymer molecular dynamics (RPMD), ring-polymer instanton (RPI) methods, and classical molecular dynamics. By conducting simulations across a wide range of temperatures and friction strengths, we can identify the various regimes that govern the reactive dynamics. At high temperatures, in addition to the spatial-diffusion and energy-diffusion regimes predicted by Kramer’s rate theory, a (coherent) tunnelling-dominated regime is identified at low friction. At low temperatures, incoherent tunnelling dominates most of Kramer’s curve, except at very low friction when coherent tunnelling becomes dominant. Unlike in classical mechanics, the bath’s influence changes the equilibrium time-independent properties of the system, leading to a complex interplay between spatially dependent friction and nuclear quantum effects even at high temperatures. More specifically, a realistic friction profile can lead to an increase (decrease) of the quantum (classical) rates with friction within the spatial-diffusion regime, showing that classical and quantum rates display qualitatively different behaviours. Except at very low frictions, we find that RPMD captures most of the quantum effects in the thermal reaction rates.

I. INTRODUCTION

The accurate modelling of chemical rates in dissipative environments is of fundamental importance to chemistry, physics, and biology [1–3]. In many systems, the reactive process can be approximated by the time evolution of a reaction coordinate coupled to a thermalizing and fluctuating environment. A simple realization of this picture is obtained with system-bath models, where the system coordinates are coupled to numerous harmonic bath degrees of freedom and the average dynamics of the system is fully governed by the bath temperature and the friction kernel [4, 5]. The first step towards accurate theoretical predictions is thus to ensure that the friction kernel is an appropriate representation of the underlying dynamics.

A key assumption often made in constructing system-bath models is to neglect the influence of the reaction coordinate on the friction kernel by linearizing the system-bath coupling. However, this approximation proves inaccurate for a variety of dynamical processes, including simple Lennard-Jones fluids [6, 7], proton-transfer reactions in the condensed phase [8], and adsorption at interfaces [9]. Another interesting instance of position-dependent friction occurs in the dynamics of atoms and small molecules near metals. In these systems, the movement of the nuclei can induce non-equilibrium fluctuations of the electrons within the metal, generating (electronic) frictional forces [10–13] that significantly modify the nuclear dynamics [14, 15]. This type of spatially-dependent friction (SDF) is especially relevant when

molecules approach interfaces, since the frictional force goes from zero in the vacuum to a finite value at the metal [15, 16].

Several studies have highlighted significant deviations between linear and non-linear models [17–23]. For example, Pollak-Grabert-Hänggi (PGH) theory has been extended to address SDF [21–23], and Voth has developed an effective Grote-Hynes theory [20]. In the strong-damping limit, both approaches calculate an average spatial modification of the friction coefficient near the barrier top and introduce it in expressions derived from position-independent theories. In this way, it has been found that a spatial antisymmetric reaction-coordinate dependence of the friction profile around the transition state leads to a negligible modification of chemical reaction rates [24], even when the coupling is strongly non-linear.

In most of these studies, nuclei are considered to be classical (Newtonian) particles. However, tunnelling and zero-point energy can change the reaction rate by several orders of magnitude and fundamentally modify its temperature dependence. It is generally accepted that coupling to a bath diminishes the magnitude of nuclear quantum effects (NQEs) [4, 25]. Most of the previous work on system-bath models, including formal analytical approaches [2, 3] and numerically accurate quantum calculations [26–28], have been limited to position-independent friction. As a result, the effects of SDF on quantum reaction rates remained overlooked with a few important exceptions. At high temperatures, approximate numerical studies reported by Navrotskaya and Geva have shown that a non-bilinear system-bath coupling can lead to an enhancement of quantum reaction rates [29], and Antoniou and Schwartz reported a reduction of kinetic isotope effects in similar scenarios [8]. At

* Email: yl899@cam.ac.uk

low temperatures, some of the present authors reported recently that an SDF profile can steer nuclear tunnelling at low temperatures [30]. Thus, a systematic study of the interplay of SDF and quantum dynamics over extended friction and temperature regimes has remained elusive.

In this article, we calculate quantum reaction rates for representative system-bath models with SDF, in regimes ranging from activated barrier crossing to deep tunnelling. We report numerically exact quantum rates at finite temperatures and use approximate methods based on imaginary-time path integrals to rationalize the results and elucidate the different rate-determining mechanisms for quantum and classical rates.

II. THEORY AND METHODS

A. Calculation of Thermal Rate Constants

Let us consider a system that can be divided into a reactant and a product region. The quantum thermal rate constant, $k_Q(T)$, of a generic "reactant" \rightarrow "product" reaction can be expressed as [31–33]

$$k_Q(T) = \frac{1}{Q_r(\beta)} c_{\text{fs}}(\beta, t) \Big|_{t>\tau}, \quad (1)$$

where $\beta = (k_B T)^{-1}$ is the inverse temperature, $Q_r(\beta) = \text{Tr}[e^{-\beta \hat{H}} (1 - \hat{h})]$ is the reactant partition function, \hat{H} is the Hamiltonian of the system, and \hat{h} is the quantum projection operator onto the product states. The flux-side correlation function is defined as

$$c_{\text{fs}}(\beta, t) = \text{Tr}[e^{-\beta \hat{H}/2} \hat{F} e^{-\beta \hat{H}/2} \hat{h}(t)], \quad (2)$$

where $\hat{F} = \frac{i}{\hbar} [\hat{H}, \hat{h}]$ is the flux operator and $\hat{h}(t) = \exp(i\hat{H}t/\hbar) \hat{h} \exp(-i\hat{H}t/\hbar)$ at time t .

The $t > \tau$ condition in Eq. 1 should be interpreted as the plateau time by which the correlation function reaches a constant value. The existence of such a plateau requires a well-defined separation of timescales such that thermal fluctuations that take particles out of the wells to the barrier top are rare events in comparison with the rapid short-time dynamics that relax $c_{\text{fs}}(\beta, t)$ to the plateau [34]. A refined formula for cases when the free-energy barrier is comparable to $k_B T$ was derived in Ref. 28 and 35.

B. Multi-configuration Time-dependent Hartree

The multi-configuration time-dependent Hartree (MCTDH) method is a wavefunction method for solving the time-dependent Schrödinger equation for multidimensional systems composed of distinguishable particles [36–38]. It employs a time-dependent basis to expand optimally (in a variational sense) the system

wave function, $|\Psi(t)\rangle$, and thus mitigate the exponential scaling problem affecting standard basis set methods. Specifically, the MCTDH wavefunction takes the form of a linear combination of products of single-particle functions (SPFs) $|\phi_j^{(k)}(t)\rangle$, one for each "mode" k ,

$$|\Psi(t)\rangle = \sum_J A_J(t) \prod_k |\phi_{j_k}^{(k)}(t)\rangle, \quad (3)$$

and both the expansion coefficients A_J and the SPFs are time-evolved according to variational equations of motion [36–38]. In the above expression $J = (j_1, \dots, j_k, \dots, j_F)$ is a multi-index and $j_k = 1, \dots, n_k$ labels the SPFs used for the k^{th} mode. The modes represent either single degrees of freedom of the system or a group thereof. In the multi-layer extension [36–38] of MCTDH (known as ML-MCTDH) the SPFs are taken to be high-dimensional and are further expanded in MCTDH form employing lower-dimensional SPFs, which in turn can be similarly expanded. This generates a hierarchical construction, a "multi-layer tree", which is terminated with low-dimensional SPFs that are directly expanded on a grid or a basis-set (the so-called primitive grid). This gives the wavefunction a rather flexible structure which makes possible the treatment of quantum systems with several hundred degrees of freedom, provided the Hamiltonian takes a relatively simple form [39, 40].

ML-MCTDH has been successfully applied to the calculation of quantum thermal rate constants in condensed-phase problems [28, 30, 41]. In these calculations, the traces appearing in $Q_r(\beta)$ and in Eq. 2, c_{fs} , are evaluated stochastically. This entails their replacement with an incoherent sum over a finite number (typically some hundreds) of representative elements from the Hilbert space of the system, which are selected stochastically using an importance sampling technique and later handled with ML-MCTDH. Specifically, the resulting "Monte-Carlo wavepacket" procedure can be summarized as follows. In the first step, a sample of pure states $\{|\Phi_i\rangle\}_i$ is drawn from the thermal equilibrium state of the (uncoupled) bath, and is combined with special system states $\{|\phi_\nu\rangle\}_\nu$ to form representatives of the total system, $|\Psi_I\rangle = |\Phi_i\rangle |\phi_\nu\rangle$. In the second step, the $|\Psi_I\rangle$ are propagated in imaginary-time using the full Hamiltonian so that they thermalize at the given temperature, $|\Psi_I^\beta\rangle = e^{-\beta \hat{H}/2} |\Psi_I\rangle$. Finally, the $|\Psi_I^\beta\rangle$ are propagated in real-time with the same Hamiltonian, $|\Psi_I^\beta\rangle \rightarrow |\Psi_I^\beta(t)\rangle$, and used to compute appropriate expectation values from which the flux-side correlation function can be easily obtained. Calculation of the reactant partition function proceeds similarly, and is simpler, since it does not require any real-time propagation. This is the strategy developed by Craig *et al.* in Ref. 28, where the interested reader can find the necessary details. Here, we use mainly the implementation described in our previous article, Ref. 30, with a few modifications that are described in Sec. III B.

C. Ring Polymer Molecular Dynamics

Ring polymer molecular dynamics (RPMD) is an approximation rooted in the (imaginary-time) path integral formulation of quantum mechanics. It utilizes a classical time evolution in an extended ring-polymer phase space to approximate the effects of quantum thermal fluctuations on the dynamics of condensed-phase systems [42, 43].

In the following, we consider the ring polymer Hamiltonian of an $F + 1$ -dimensional system given by

$$H_P(\mathbf{p}, \mathbf{q}) = U_P(\mathbf{q}) + \sum_{j=0}^F \sum_{k=1}^P \frac{\left(p_j^{(k)}\right)^2}{2m_j}, \quad (4)$$

where

$$U_P(\mathbf{q}) = \sum_{j=0}^F \sum_{k=1}^P \left[\frac{m_j \omega_P^2}{2} \left(q_j^{(k)} - q_j^{(k+1)} \right)^2 \right] + \sum_{k=1}^P V \left(q_0^{(k)}, q_1^{(k)}, \dots, q_F^{(k)} \right). \quad (5)$$

and $\mathbf{q}^{(k)} = \{q_0^{(k)}, q_1^{(k)}, \dots, q_F^{(k)}\}$ represent the positions of the k -th ring-polymer bead, $\mathbf{q} = \{\mathbf{q}^{(1)}, \mathbf{q}^{(2)}, \dots, \mathbf{q}^{(P)}\}$ is a short form denoting all the position coordinates, $\mathbf{p}^{(k)}$ and \mathbf{p} are similarly defined for the momenta, m_j is the mass of the j -th degree of freedom, V is the potential energy surface (PES), and $\omega_P = (\beta_P \hbar)^{-1}$, with $\beta_P = \beta/P$. The RPMD approximation to the exact quantum rate constant is given by [44, 45]

$$k_Q(T) \approx k_{\text{RPMD}}(T) = \lim_{P \rightarrow \infty} k^{(P)}(T) = \lim_{P \rightarrow \infty} \frac{1}{Q_r^{(P)}} c_{\text{fs}}^P(\beta, t) \Big|_{t > \tau}, \quad (6)$$

where τ is the plateau time beyond which $c_{\text{fs}}^P(\beta, t)$ has become time-independent. Here, the reactant partition function, $Q_r^{(P)}$, is the P -bead path-integral approximation to its exact quantum counterpart, and

$$c_{\text{fs}}^P(t) = \frac{1}{(2\pi\hbar)^{FP}} \int d\mathbf{p} \int d\mathbf{q} e^{-\beta_P H_P} \delta[s(\mathbf{q})] v_s(q) h[s(\mathbf{q}(t))] \quad (7)$$

is the ring-polymer flux-side time-correlation function, in which $s(\mathbf{q})$ is a dividing surface between reactant and products, v_s is the velocity component orthogonal to s , and h is a heaviside step function. The time evolution of $\mathbf{q}(t)$ is generated using the classical equations of motion obtained from the ring-polymer Hamiltonian of Eq. 4.

The RPMD rate constant, $k_{\text{RPMD}}(T)$, is clearly artificial but it has a number of important properties which ensure that it is often a good approximation to the exact quantum rate: i) it is exact in the harmonic and classical limits [44, 45], ii) it is independent of the position of the

dividing surface s , and iii) if s is constructed to be invariant under cyclic permutation of the polymer beads, the corresponding RPMD TST rate, $k_{\text{RPMD}}^\ddagger(T)$, (obtained by taking $\tau \rightarrow 0^+$ in Eq. 6) gives the exact quantum flux through the dividing surface in the limit $t \rightarrow 0^+$ [46], which correctly accounts for the dominant effects of instantons in the deep-tunnelling regime [47]. If the barrier is symmetric (as is the case for the systems treated here [48]), the optimal dividing surface $s(\mathbf{q})$ is a function of just the ring-polymer centroid $\mathbf{q}^c = \{q_0^c, q_1^c, \dots, q_F^c\}$, which has components

$$q_j^c = \sum_{k=1}^P q_j^{(k)}, \quad (8)$$

and in this case $k_{\text{RPMD}}^\ddagger(T)$ is identical to the centroid-TST rate [49, 50]. Because of its computational efficiency, RPMD has been used to compute rates in complex systems [43, 51], including polyatomic gas-phase reactions [52–57] and protein rearrangement reactions [58].

D. Ring Polymer Instanton Method

The ring polymer instanton (RPI) method [47, 59] is an efficient semi-classical method for computing tunnelling rates in the "deep tunnelling" regime

$$T < T_c^\circ = \frac{\hbar\omega^\ddagger}{2\pi}, \quad (9)$$

in which the saddle point on $U_P(\mathbf{q})$ is delocalised into an imaginary-time periodic orbit known as the "instanton" [60, 61]. We note that this expression applies to barriers that resemble parabolas close to the barrier top; for flatter barriers, the determination of T_c is not so simple [62, 63]. In the RPI method, the instanton is located by running standard saddle point search algorithms on $U_P(\mathbf{q})$ [64–66]. The large computational cost associated with the sampling procedure is thus replaced by a few geometry optimization and Hessian calculations. The tunnelling rate can be expressed as [61]

$$k_{\text{inst}}(T) = \frac{1}{Q_r^{(P)}} \frac{1}{\beta_P \hbar} \sqrt{\frac{B_P(\bar{\mathbf{q}})}{2\pi\beta_P \hbar^2}} Q_{\text{vib}} e^{-S_P(\bar{\mathbf{q}})/\hbar}, \quad (10)$$

where

$$S_P/\hbar = \beta_P U_P, \quad (11)$$

$\bar{\mathbf{q}}$ is the position vector corresponding to the optimized instanton geometry, which can be identified as the discretized version of the Euclidean action with U_P given by Eq. 5, and

$$B_P(\bar{\mathbf{q}}) = \sum_{i=1}^F \sum_{k=1}^P m_i (\bar{q}_i^{(k+1)} - \bar{q}_i^{(k)})^2. \quad (12)$$

The instanton vibrational partition function, Q_{vib} , is approximated by

$$Q_{\text{vib}} = \prod_k \frac{1}{\beta_P \hbar |\lambda_k|}, \quad (13)$$

where λ_k are the non-zero eigenvalues of the ring-polymer dynamical matrix [67].

The RPI method has been successfully applied to systems containing hundreds of atoms using accurate *ab initio* potential energy surfaces [67–71]. The RPI rate $k_{\text{inst}}(T)$ typically agrees with the exact quantum rate to within a factor of two [61].

III. SIMULATION DETAILS

A. System-Bath Model with Position-dependent Friction

We consider a system-bath model described by the following PES [44, 72]

$$V(q; x_1, \dots, x_F) = V_{\text{sys}}(q) + \sum_{j=1}^F \frac{m_j \omega_j^2}{2} \left(x_j - \frac{c_j g(q)}{m_j \omega_j^2} \right)^2, \quad (14)$$

where q and $\{x_1, \dots, x_F\}$ correspond to the (1D) system and bath degrees of freedom, respectively, and V_{sys} refers to the PES of the system in the absence of a bath. The bath is described by a spectral density

$$J(q, \omega) = \left(\frac{\partial g(q)}{\partial q} \right)^2 \frac{\pi}{2} \sum_{j=1}^F \frac{c_j^2}{m_j \omega_j} (\delta(\omega - \omega_j) + \delta(\omega + \omega_j)), \quad (15)$$

where $g(q)$ determines the position-dependence of the system-bath coupling. Equivalently, the system-bath coupling can be subsumed in a position- and frequency-dependent friction kernel, $\tilde{\eta}(q, \lambda)$, which is related to the bath spectral density by

$$\tilde{\eta}(q, \lambda) = \frac{1}{\pi} \int_{-\infty}^{\infty} d\omega \frac{J(q, \omega)}{\omega} \frac{\lambda}{\omega^2 + \lambda^2}, \quad (16)$$

and is position-independent when $g(q) = q$. In this work, we use simple models for V_{sys} and $\tilde{\eta}$. For V_{sys} , we use the "DW1" double-well model of Topaler and Makri [72],

$$V_{\text{sys}}(q) = -\frac{1}{2} m \omega^{\ddagger 2} q^2 + \frac{m^2 \omega^{\ddagger 4}}{16V_0} q^4, \quad (17)$$

where $\omega^{\ddagger} = 500 \text{ cm}^{-1}$, $V_0 = 2085 \text{ cm}^{-1}$, and m is the mass of atomic hydrogen. For the system-bath coupling, we use

$$g(q) = q[1 + \epsilon_1 \exp(-(q/\delta)^2/2) + \epsilon_2 \tanh(q/\delta)], \quad (18)$$

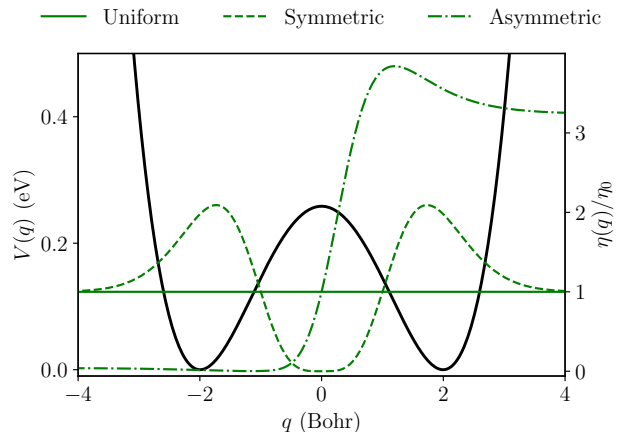


FIG. 1. Friction profiles for the uniform (solid green line), symmetric (dashed) and asymmetric (dot-dashed) models of Tab. I, with the DW1 potential energy (black line).

where δ , ϵ_1 and ϵ_2 are positive real numbers. The spectral density is taken to be Ohmic with an exponential cutoff,

$$J^{\text{Ohm}}(q, \omega) = \left(\frac{\partial g(q)}{\partial q} \right)^2 \eta_0 \omega e^{-\omega/\omega_c}, \quad (19)$$

where η_0 is the Ohmic friction coefficient and $\omega_c = 500 \text{ cm}^{-1}$ is a frequency cutoff; when $g(q) = q$, $J^{\text{Ohm}}(q, \omega)$ reduces to the position-independent spectral density employed in the DW1 model of Ref. 72.

The factorization of the spectral density into position-dependent and frequency-dependent factors, usually referred to as separable coupling or uniform coupling [22, 73], assumes that the dynamical time scale is independent of the value of the reaction coordinate. This approximation is justified in most cases since, to lowest order, the system-bath and bath-bath couplings determine respectively the magnitude and the timescale of the friction kernel [22]; it has also been shown numerically to give a good approximation to electronic friction in several metals [30].

We consider three friction models, one model with position-independent coupling, and two models with position-dependent coupling. The model parameters are summarized in Tab. I. In Fig. 1, we plot the PES and friction coefficients along with the reaction coordinate. The uniform model has a constant friction profile and serves as a reference from which we can evaluate the impact that non-linear couplings (non-uniform friction) have on

Model	ϵ_1	ϵ_2	δ
Uniform	0.0	0.0	1.0
Symmetric	-1.0	0.0	1.0
Asymmetric	0.0	0.8	0.5

TABLE I. Parameters of the friction models employed in this work.

the thermal rate. The symmetric model has a lower friction coefficient in the vicinity of the transition state and a larger one at the reactant and product wells. This friction profile resembles one recently constructed for hydrogen diffusion reactions in metals [30], for a proton-transfer reaction in liquid methyl chloride [8], and the one studied by Navrotskaya and Geva [29]. The asymmetric model has vanishing friction in the reactant well and larger friction in the product well, similar to the models employed by Straus and others [18, 22, 29]. Note that this model presents the same friction value as the uniform case at the transition state.

B. ML-MCTDH Calculations

The ML-MCTDH calculations were implemented using the Heidelberg package [74]. Except for the details given below, these calculations followed Ref. 30 (Supplementary Information), which is an implementation of the Monte Carlo wavepacket strategy of Craig *et al.* [28]. The bath was described with $F = 50$ modes, using the logarithmic discretization of Ref. 75, and its (uncoupled) thermal equilibrium state was sampled to extract between 256 and 512 realizations, n_B , for each temperature, T . These bath states were combined with n_S system states to define a running sample of $n_B \times n_S$ wavepackets for each value of the temperature and of the coupling strength. The resulting $F + 1$ -dimensional wavepackets were propagated with ML-MCTDH, in both imaginary and real-time, using a single ML-tree structure. The latter was obtained after extensive tests at the extremes of the temperature-coupling strength intervals of interest (see Ref. 30 [Supplementary Information] for details). The choice of the "bare" system states depends on the type of calculation—whether it is for the reactant partition function or the flux-side correlation function—and must be optimized to reduce the overall computational cost. This choice is particularly crucial for the flux-side calculation, since the flux operator \hat{F} is intrinsically of high-rank, and could require many states if represented in the usual spectral form, $\hat{F} = \sum_{\nu} \nu |\nu\rangle \langle \nu|$. The trick [28] is to observe that its Boltzmannized version \hat{F}_{β} is of low rank, and therefore \hat{F} is better rewritten as $\hat{F} = e^{\beta\hat{H}_S/2}\hat{F}_{\beta}e^{\beta\hat{H}_S/2}$ where \hat{H}_S is the system Hamiltonian. Typically, \hat{F}_{β} is well represented by a small number of (time-reversed conjugate) pairs of eigenstates; in our calculations, $n_S = 2$ was found to be sufficient, so that $\hat{F}_{\beta} \approx \nu_{\beta} |\nu_{\beta}\rangle \langle \nu_{\beta}| - \nu_{\beta} |\bar{\nu}_{\beta}\rangle \langle \bar{\nu}_{\beta}|$, where ν_{β} is the largest-magnitude eigen-flux and the bar denotes application of time-reversal. The drawback with this approach is that the reverse imaginary-time propagation needed to define the system states, $|\phi_{\beta}\rangle = e^{+\beta\hat{H}_S/2} |\nu_{\beta}\rangle$, can be numerically unstable due to high energy states in \hat{H}_S which are, however, irrelevant for the dynamics. To circumvent this problem, we exploit $\hat{F}e^{-\beta\hat{H}_S/2} = e^{\beta\hat{H}_S/2}\hat{F}_{\beta}$ to write $\nu_{\beta} |\phi_{\beta}\rangle = \hat{F}e^{-\beta\hat{H}_S/2} |\nu_{\beta}\rangle$, which only requires the

numerically stable imaginary-time propagation $e^{-\beta\hat{H}_S/2}$ and the application of the bare flux operator \hat{F} . This amounts to the following formal manipulation of the flux operator

$$\begin{aligned} \hat{F} &= \hat{F}e^{-\beta\hat{H}_S/2}\hat{F}_{\beta}^{-1}e^{-\beta\hat{H}_S/2}\hat{F} \\ &\approx \sum_{\nu} \nu_{\beta}^{-1}\hat{F}e^{-\beta\hat{H}_S/2} |\nu_{\beta}\rangle \langle \nu_{\beta}| e^{-\beta\hat{H}_S/2}\hat{F} \end{aligned} \quad (20)$$

where the sum is restricted to the largest-magnitude eigenvalues of the Boltzmannized flux operator; i.e., \hat{F}_{β}^{-1} is replaced by the pseudo-inverse of a low-rank approximation of \hat{F}_{β} .

C. RPMD, Classical and RPI Simulations

The ring-polymer potential used in RPMD and RPI simulations was obtained by substituting Eq. 14 into Eq. 5, such that each imaginary-time slice contains one system coordinate and the corresponding modes of the discretized bath. The RPMD rate constants were computed using the Bennett-Chandler approach [76, 77] which is based on the factorization

$$k_{\text{RPMD}}(T) = k_{\text{RPMD}}^{\ddagger}(T; s)\kappa_{\text{RPMD}}(T; s), \quad (21)$$

where $\kappa_{\text{RPMD}}(T; s)$ is the RPMD transmission coefficient [52] (i.e. the fraction of trajectories initiated at the dividing surface which remain on the product side at $t > \tau$). Note that $k_{\text{RPMD}}^{\ddagger}(T; s)$ and $\kappa_{\text{RPMD}}(T; s)$ depend on the specific choice of the dividing surface, s , whereas $k_{\text{RPMD}}(T)$ does not. Unless specified otherwise, we take $s(\mathbf{q}^c) = q_0^c - q_0^{\ddagger}$, where q_0^{\ddagger} is the classical transition state and q_0^c is the projection of the centroid along the system coordinate, so that $v_s = p_0^c/m_0$, where p_0^c is the momentum conjugate to q_0^c . The terms on the right-hand side of Eq. 21 can then be written

$$k_{\text{RPMD}}^{\ddagger}(T; s) = \left(\frac{k_B T}{2\pi m}\right)^{1/2} \frac{\langle \delta(q_0^c - q_0^{\ddagger}) \rangle}{\langle h(q_0^{\ddagger} - q_0^c) \rangle}, \quad (22)$$

and

$$\kappa_{\text{RPMD}}(T; s) = \kappa_{\text{RPMD}}(T, t; s) \Big|_{t>\tau} \quad (23)$$

with

$$\kappa_{\text{RPMD}}(T, t; s) = \frac{\langle \delta(q_0^c - q_0^{\ddagger})(p_0^c/m)h(q_0^c(t) - q_0^{\ddagger}) \rangle}{\langle \delta(q_0^c - q_0^{\ddagger})(p_0^c/m)h(p_0^c) \rangle}, \quad (24)$$

where $\langle \dots \rangle$ denotes the average over the canonical ensemble determined by H_p (see Eq. 4), and τ is the plateau time previously mentioned.

We computed $k_{\text{RPMD}}^{\ddagger}$ by thermodynamic integration [52], and κ_{RPMD} by sampling from a thermal distribution with the ring-polymer centroid pinned at the barrier

top. The spectral density was discretized using the same logarithmic discretization employed for the ML-MCTDH calculations [75]. A total of 9, 12 and 64 bath modes were required to converge the uniform, symmetric, and asymmetric models, respectively. We used 16 and 64 beads for the simulations at 300 K and 50 K, respectively.

The classical rate constants k_{cl} were calculated similarly to the RPMD rate constants by multiplying the classical TST rate k_{cl}^\ddagger with the transmission coefficient $\kappa_{\text{cl}}(t)$.

The RPI simulations were carried out using the Nichols saddle-point search algorithm [65]; the number of replicas and the number of bath modes were converged to within graphical accuracy. Note that some of the authors have developed a version of the RPI method which includes the bath implicitly [78], but for consistency we used the same explicit (discretized) bath for the RPI calculations as for the ML-MCTDH and RPMD calculations.

To facilitate comparison with previous work, we will sometimes present the "transmission coefficients"

$$\bar{\kappa}(T) = \frac{k(T)}{k_{\text{ha,cl}}^\ddagger(T)}, \quad (25)$$

in place of the quantum, RPMD or classical rate constants $k(T)$, where $k_{\text{ha,cl}}^\ddagger$ is the harmonic approximation to the classical TST rate. To avoid confusion in what follows we always denote the coefficients of Eq. 25 with a bar, to distinguish them from the true transmission coefficients, κ_{RPMD} and κ_{cl} , defined as in Eq. 21.

IV. RESULTS

We start by presenting the ML-MCTDH quantum rate constants $k_Q(T)$ as a function of temperature. Figure 2 plots $k_Q(T)$ between 50 K and 300 K for $\eta_0/m\omega^\ddagger$ between 0.05 and 2.00; note that the rate is plotted only when the flux-side correlation function shows a clear plateau. The results for the uniform friction model are shown in panel a in Fig. 2 along with the results reported by Topaler and Makri (TM) using the quasiadiabatic propagator path integral (QUAPI) [72]. The two sets of results are in very close agreement. A further comparison with reaction rates reported by Craig [28] is presented in Fig. S1 and shows equally good agreement.

The three models show an exponential decrease of the rate with temperature down to $\sim 100\text{K}$ where some of the simulations with the lowest friction reach a plateau characteristic of deep tunnelling. At low temperatures, the rates decrease monotonically with the increase of friction in all three models, showing that (as expected) dissipative effects inhibit quantum tunnelling, irrespective of the friction profile. At high temperatures, the rates follow a non-monotonic behaviour with varying friction, characteristic of Kramers-like behaviour [1]. In the following Sections, we analyze in more detail the dynamics at high and low temperatures.

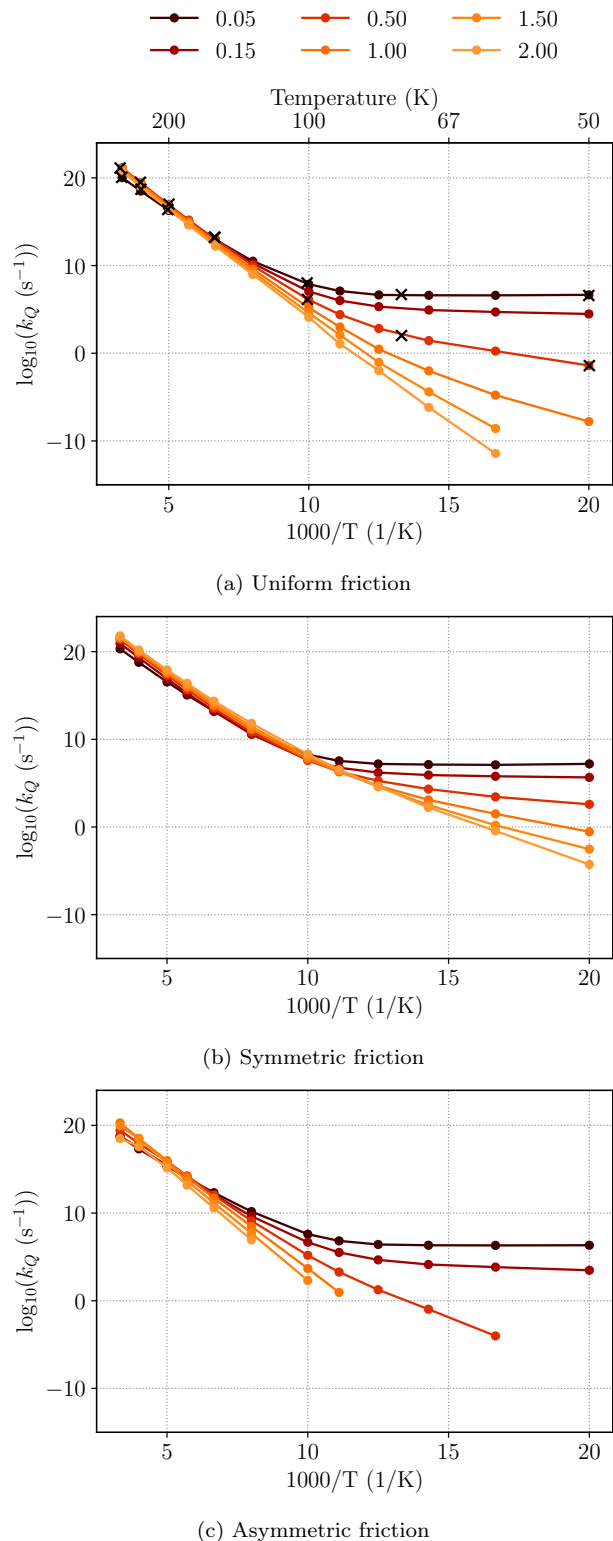


FIG. 2. ML-MCTDH rate constants, $k_Q(T)$, for the three friction models of Tab. I, for values of the reduced friction from $\eta_0/m\omega^\ddagger=0.05$ (blue) to $\eta_0/m\omega^\ddagger=2.00$ (pink). Also shown are the QUAPI results of Ref. 72 (black crosses).

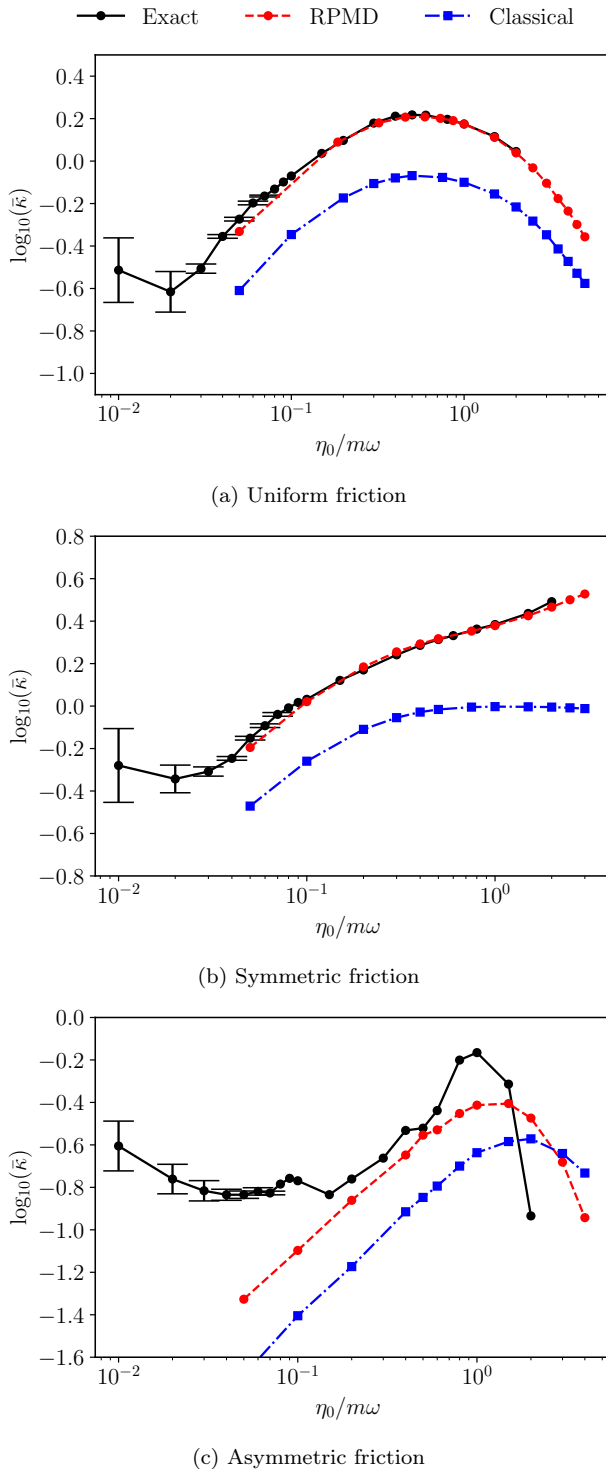


FIG. 3. Transmission coefficients $\bar{\kappa}(T = 300 \text{ K})$ for the (a) uniform friction, (b) symmetric friction, and (c) asymmetric friction models, obtained from the corresponding ML-MCTDH, RPMD and classical rate constants using Eq. 25. The error bars reported for the ML-MCTDH results with the lowest friction values correspond to the variation of the flux-side correlation functions during the last 100 fs of simulation (see Fig. S2). Only error bars representing errors larger than 1% are shown.

A. Quantum Effects at High Temperatures

1. Overview

Figure 3a shows the ML-MCTDH results obtained at 300 K for the uniform friction model. These results are consistent with previous studies on this system, showing the characteristic Kramers' turnover [1, 2] separating the underdamped (energy-diffusion) and overdamped (spatial-diffusion) regimes. In the overdamped regime, $\eta_0/m\omega^\ddagger > 0.6$, the rate decreases monotonically with friction since the bath hinders the reactant from diffusing over the barrier. In the underdamped regime, $0.05 < \eta_0/m\omega^\ddagger < 0.3$, the rate increases approximately linearly with the coupling strength since it is proportional to the rate at which energy can be transferred from the thermal fluctuations of the bath to the reaction coordinate.

According to classical rate theories, at even weaker coupling, the rate should tend to zero. However, the ML-MCTDH simulations show another (purely quantum) regime, where the rate remains approximately constant within our uncertainties. Representative flux-side time-correlation functions $c_{fs}(t)$ illustrating the dynamics in the three regimes are plotted in Fig. S2, where the curves corresponding to the lowest friction couplings show the characteristic oscillation of coherent tunnelling. The transition from the tunnelling-dominated to the energy-diffusion regime at $\eta_0/m\omega^\ddagger = 0.02$ moves towards larger values of $\eta_0/m\omega^\ddagger$ upon decreasing the temperature (see Fig. S3), thus shrinking the energy-diffusion regime until it disappears at sufficiently low temperature. Similar behaviour has been reported in recent studies by others [79, 80]. The error bars reported in Fig. 3 could not be reduced further due to the appearance of bath recurrences (see Fig. S4). However, we performed further ML-MCTDH calculations at 200 K, where this problem is less severe, and found that within the tunnelling-dominated regime, the reaction rates indeed increase when the friction is reduced (see Fig. S5). Thus, in the low coupling limit, the increase of the dissipation strength reduces the rates by suppressing the (coherent) tunnelling [4, 73, 81].

Figure 3b shows the ML-MCTDH results for the symmetric friction model. For $\eta_0/m\omega^\ddagger > 0.4$, the rate increases approximately linearly with $\eta_0/m\omega^\ddagger$. This monotonic growth in the rate with $\eta_0/m\omega^\ddagger$ arises because this model has zero friction in the region of the barrier (see Fig. 1); the addition of a small amount of friction to the barrier would cause an eventual turnover of the rate at sufficiently high $\eta_0/m\omega^\ddagger$. Nonetheless, this monotonic growth depicted in Fig. 3b cannot be explained away as a simple shift of the Kramers' turnover to higher friction values; we show below that it is a genuine quantum effect.

Figure 3c shows the ML-MCTDH results for the asymmetric model. The ML-MCTDH calculations were much harder to converge for this model owing to the small system-bath coupling in the reactant well; tests suggest that, unlike the other two models, the ML-MCTDH cal-

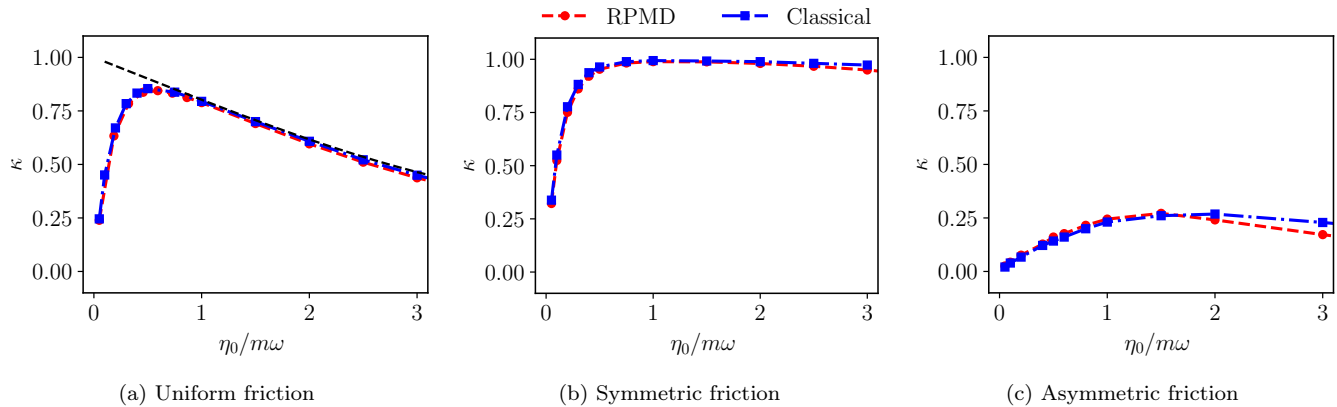


FIG. 4. Transmission coefficients $\kappa(T = 300 \text{ K})$, as defined in Eq. 21-24, calculated for the (a) uniform friction, (b) symmetric friction, and (c) asymmetric friction models, using RPMD (red) and classical MD (blue). Panel (a) also shows the (classical) Grote-Hynes transmission factor [83, 84] (black dashed line).

culations may not have fully converged with respect to the number of bath modes. Full convergence would require the development and optimization of a new ML-MCTDH tree structure which was not performed due to the prohibitive computational cost. Despite these limitations, the ML-MCTDH calculations are sufficiently well converged to show that the asymmetric model gives rise to the same three kinetic regimes as the uniform model. The Kramers' turnover is shifted to a slightly higher value of $\eta_0/m\omega^\ddagger \sim 0.9$, after which there is a much steeper drop in $\kappa(T)$ (which may be an artefact of the incomplete convergence just mentioned). The transition between the tunnelling-dominated and energy-diffusion regimes occurs at $\eta_0/m\omega^\ddagger \sim 0.1$, a value five times larger than the one obtained for the uniform model. The similarity of the qualitative shapes of the uniform and asymmetric curves for the intermediate and large friction regimes suggests that the SDF in the asymmetric model could be approximated as an effective spatially independent friction, as in the effective Grote-Hynes theory of Voth [20].

To interpret the ML-MCTDH results, especially the monotonic growth of the rate with $\eta_0/m\omega^\ddagger$ in the symmetric model, we compare with the results of classical and RPMD calculations. Figure 3 shows the RPMD rates calculated for the three models at 300K. For the uniform model, the RPMD simulations are in good agreement with the ML-MCTDH results in the underdamped and overdamped regimes. The RPMD calculations were difficult to converge in the tunnelling dominated regime ($\eta_0/m\omega^\ddagger < 0.05$), and in any case cannot be expected to work here, where the dynamics is dominated by real-time quantum coherence. The classical rates have the same Kramers' turnover as the RPMD rates, but are smaller by roughly a factor of two. The RPMD results for the symmetric model are also in good agreement with the ML-MCTDH results, showing the same monotonic increase in the rate with friction for $\eta_0/m\omega^\ddagger > 0.6$; the classical results, however, do not reproduce this feature, giving

instead a plateau for $\eta_0/m\omega^\ddagger > 0.6$. For the asymmetric model, the RPMD and ML-MCTDH results differ appreciably. In the underdamped regime, these differences can be attributed to the neglect by RPMD of real-time coherence and coupling of the centroid to the Matsubara fluctuation modes [82]; in the overdamped regime, while both methods show the same qualitative turnover behaviour, their difference is most likely due to the previously mentioned lack of convergence of the ML-MCTDH calculations.

2. Analysis of Quantum Effects

The qualitative differences between the RPMD and classical rates in Fig. 3 can be analysed in terms of the dynamical and statistical contributions to the rate defined by Eqs. 21-24, namely the transmission factors $\kappa(T)$ and the TST rates $k^\ddagger(T)$. We can further factorise the latter into

$$k_{\text{RPMD}}^\ddagger(T) = \left(\frac{k_B T}{2\pi m} \right)^{1/2} e^{-\beta \Delta \mathcal{A}_{\text{RPMD}}^\ddagger} \frac{\langle \delta(q_0^c - \bar{q}_0) \rangle}{\langle h(q_0^\ddagger - q_0^c) \rangle}, \quad (26)$$

where

$$\Delta \mathcal{A}_{\text{RPMD}}^\ddagger = \mathcal{A}_{\text{RPMD}}(q_0^\ddagger) - \mathcal{A}_{\text{RPMD}}(\bar{q}_0), \quad (27)$$

and

$$\mathcal{A}_{\text{RPMD}}(q_0) = -\frac{1}{\beta} \ln \langle \delta(q_0^c - q_0) \rangle \quad (28)$$

is the free energy difference needed to move the centroid from the bottom of the well, \bar{q}_0 , to the barrier top, q_0^\ddagger .

The transmission coefficients $\kappa(T)$ are plotted in Figure 4, and the free energy differences $\Delta \mathcal{A}_{\text{RPMD}}^\ddagger$ in Figure 5. Fig. 4 shows that $\kappa_{\text{RPMD}}(T)$ is very close to $\kappa_{\text{cl}}(T)$ for the uniform and symmetric models. In other

words, there are almost no quantum effects in the recrossing dynamics for these two models over the entire range $\eta_0/m\omega^\ddagger > 0.05$ for which RPMD reproduces the ML-MCTDH rates (in Fig. 3). The small differences between $\kappa_{\text{RPMD}}(T)$ and $\kappa_{\text{cl}}(T)$ for the asymmetric model (Fig. 4c) are perhaps a sign that delocalisation between the zero friction and high friction halves of the potential affects the recrossing dynamics.

The strong quantum effects that cause the rates for the symmetric model to increase monotonically with $\eta_0/m\omega^\ddagger$ for $\eta_0/m\omega^\ddagger > 0.5$ (see Fig. 3b) are thus caused by the dependence of the quantum free-energy gap $\Delta\mathcal{A}_{\text{RPMD}}^\ddagger$ on $\eta_0/m\omega^\ddagger$. It is well known [4, 78] that the quantum free energy of a system-bath model depends strongly on $\eta_0/m\omega^\ddagger$: the system ring-polymer modes orthogonal to the centroid couple to their counterparts in the bath, which increases the effective polymer-spring force constants, causing the ring polymers to shrink as though the fluctuations were occurring at an effectively higher temperature, or as if the system's mass were increased. Within the harmonic approximation, and for a bath with Ohmic spectral density, the free energy of the uniform model at the bottom of the well is [4, 78] [85]

$$\mathcal{A}_{\text{RPMD}}(\bar{q}_0) = \frac{1}{\beta} \ln \left[\prod_{l=0}^{(P-1)/2} \omega_l^2 + \frac{|\omega_l|\eta_0}{m} + (\omega_{\text{well}})^2 \right] + V(q_0^\ddagger) + \text{const.}, \quad (29)$$

where $\omega_l = 2\omega_P \sin(|l|\pi/P)$ are the free ring polymer normal mode frequencies and ω_{well} is the frequency at the bottom of the well. The classical limit of Eq. 29 is obtained by taking $P = 1$, and since $\omega_{l=0} = 0$, the classical free energy is indeed friction and mass independent. Eq. 29 clearly shows that \mathcal{A} increases monotonically with the increase of friction. This dependence, which also applies to anharmonic potentials, can be rationalized in two equivalent ways: either as a renormalization of the system mass or as an increase of the quantum fluctuations.

In Fig. 5a, the classical and quantum reaction free energies at 300 K are presented. $\Delta\mathcal{A}_{\text{RPMD}}^\ddagger$ at $\eta_0=0$ is smaller than the classical one due to the zero-point energy at the reactant well. For finite values of friction, $\Delta\mathcal{A}_{\text{RPMD}}^\ddagger$ stays approximately constant for the uniform model, whereas it decreases (increases) for the symmetric (asymmetric) model. The different behaviour between the uniform and non-uniform friction models is a direct consequence of the increase of quantum free energy with friction (as approximately described by Eq. 29 using a local harmonic approximation). While the free energy at the reactant basin and transition state region increase comparably in the model with uniform friction, due to the shape of the friction profile in the symmetric model, the free energy at the reactant well increases more rapidly than at the transition state for this case. This difference leads to the monotonic decrease of the free energy barrier with friction shown in panel (a) and schematically represented in

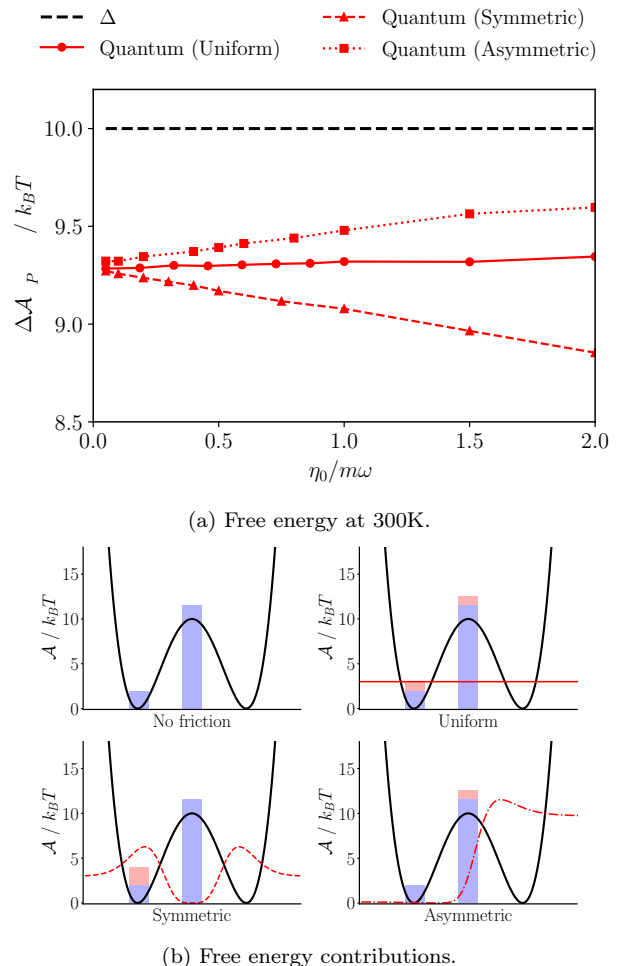


FIG. 5. Analysis of the dependence of the quantum free energy on the bath coupling strength $\eta_0/m\omega^\ddagger$ at 300 K, showing (a) the reaction free-energy $\Delta\mathcal{A}_{\text{RPMD}}^\ddagger$ for the three friction models, and (b) the free-energy at the barrier and in the well, decomposed into contributions from thermal quantum fluctuations of the pure system (blue) and the system-bath coupling (pink). $\Delta\mathcal{V}^\ddagger = V(q^\ddagger) - V(\bar{q}_0)$. Friction contributions are estimated using Eq. 29 and multiplied by a factor of four to ease visualization.

panel (b). Our results are consistent with those previously reported in Ref. 29 based on QUAPI and centroid-molecular-dynamics [86] simulations on similarly symmetric SDF profiles. The asymmetric model presents vanishing friction at the reactant basin and finite friction at the top of the barrier. An analogous argument explains the increase of $\Delta\mathcal{A}_{\text{RPMD}}^\ddagger$ with the increase of friction observed in this case (see curve in Fig. 5a and sketch in Fig. 5b).

B. Quantum Effects at Low Temperatures

Another consequence of the dependence of the free energy on the system-bath coupling is that the instanton

cross-over temperature is reduced below the value of T_c° , given in Eq. 9, to [78, 83, 87]

$$T_c(\eta_0) = T_c^\circ \left[\left(\frac{\tilde{\eta}(\omega_0)}{2m\omega^\ddagger} \right)^2 + 1 \right]^{\frac{1}{2}} - \frac{\tilde{\eta}(\omega_0)}{2m\omega^\ddagger}, \quad (30)$$

where ω_0 is the free-energy barrier frequency and the friction is evaluated at the top of the barrier[88]. For the DW1 potential, the cross-over temperature reduces from 115 K for the uncoupled system to 92 K for $\eta_0/m\omega^\ddagger = 1$. The ML-MCTDH results display a smooth transition between the high-temperature and low-temperature regimes (see Fig. S3). To simplify the discussion we focus on the results at 50 K, where the system remains in the deep tunnelling regime across the entire range of friction.

Figure 6 compares the reaction rates at 50 K using ML-MCTDH, RPMD, RPI and classical MD. In all models, the reaction rate decreases with friction in a qualitatively similar way, in contrast with the high-temperature results. The Kramers turnover is not present since it is exponentially suppressed with temperature [72, 89, 90]. The decrease of the rate with friction in the symmetric and asymmetric models is less pronounced than for the uniform coupling, suggesting that even in the deep tunnelling regime, quantum dynamics are particularly sensitive to how the frictional forces change in the vicinity of the barrier top. This difference is also observed in the centroid-free energies along the reaction pathway (see Fig. S6 in the supporting information).

Since the reaction is dominated by deep tunnelling at this temperature, the classical rates are orders of magnitude smaller than the quantum rates. RPI results are within a factor of two of the ML-MCTDH ones proving that in the deep-tunnelling regime, real-time quantum dynamics plays a minor role, except at vanishing friction strength. In this limit, namely for $\eta_0/m\omega^\ddagger < 0.05$, the ML-MCTDH rates show a marked increase with the decrease of friction, in agreement with simulations reported using hierarchical equations of motion (HEOM) for an effective two-state spin-boson model [91]. The larger discrepancy observed for the asymmetric model, reaching a factor of four at the largest computed value of friction, is probably due to the lack of convergence of the ML-MCTDH results, as discussed in the high-temperature results. RPMD systematically underestimates the RPI reaction rates, which is typical for a symmetric reaction barrier, and can be traced back to the different treatment of the unstable mode, λ_0 , in RPI and the harmonic TST version of RPMD [92]. The ratio between the RPI and harmonic RPMD-TST rates can be shown to be[92]

$$\alpha_h(\beta) = \frac{2\pi}{\beta\hbar|\lambda_0|}, \quad (31)$$

which for the uniform model varies from 4.1 at $\eta_0/m\omega^\ddagger = 0.1$ to 1.9 at $\eta_0/m\omega^\ddagger = 1.0$.

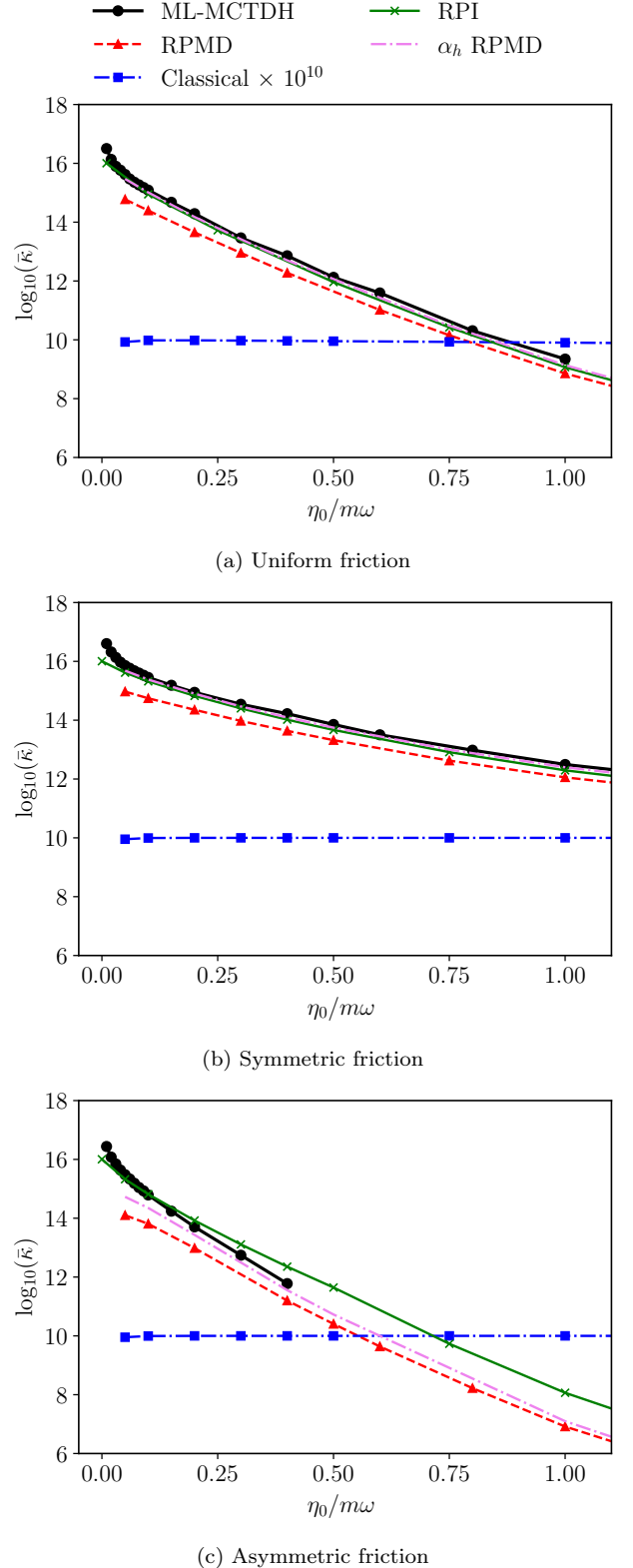


FIG. 6. Transmission coefficients $\bar{\kappa}(T = 50 \text{ K})$ for the (a) uniform friction, (b) symmetric friction, and (c) asymmetric friction models, obtained from the corresponding ML-MCTDH, RPMD, and RPI rate constants using Eq. 25. The ' α_h RPMD' coefficients were obtained by multiplying the RPMD rate constants by the $\alpha_h(\beta)$ correction factor of Eq. 31.

V. CONCLUSIONS

We have investigated the effects on Kramers'-type reactions of making the friction spatially-dependent. We carried out accurate (ML-MCTDH) and approximate (RPMD, RPI and classical) simulations on two very different spatially-dependent friction profiles (called "symmetric" and "asymmetric"). We find that the spatial dependence introduces strong quantum effects into the rate constants for both models, over the full range of friction strengths considered (which, for a uniform friction strength would encompass the full range of the Kramers' curve). However, only at very low overall friction strengths can these effects be attributed to real-time quantum dynamics. At higher friction strengths, the quantum effects are found to be static, reflecting the changes in the quantum free-energy profiles that result when the friction is made spatially-dependent. We also find tentative evidence (from the tests on the asymmetric profile) that quantum dynamical effects might play a role in systems with a steep variation between low and high friction, but these results are inconclusive (since we do not know whether the ML-MCTDH calculations have converged to the exact quantum rates for this friction profile).

Methodologically, these results imply that spatially-dependent friction models behave similarly to the commonly used system-bath models with spatially-independent friction. Thus, at low overall friction, accurate quantum methods are needed to capture the real-time coherence. Here, we used the ML-MCTDH method; hopefully, these results will be useful to others for benchmarking the variety of approximate methods, e.g. linearized semiclassical theory [93, 94], that have been successfully applied to the uniform friction case. As mentioned in the Introduction, QUAPI has already been applied to position-dependent friction baths by Navrotskaya and Geva [29], and we expect that the HEOM method [95, 96] could be similarly extended. However, once the friction is large enough to remove most of the real-time coherence (which is still in the energy-diffusion-limited Kramers' regime) then RPMD is, by construction, able

to capture all the quantum free-energy effects and thus will usually work well in this regime (except perhaps for friction profiles with steep variations—see above). This is useful to know, as RPMD is typically orders of magnitude cheaper than accurate quantum methods.

There are a variety of systems which could be modelled realistically by spatially-dependent friction and which could thus be treated using the approaches used in this article. In the low friction regime, we mention in particular optical cavities [80, 97, 98] where real-time quantum effects are thought to be important; at higher frictions, a version of RPMD has already been used to study the diffusion of light particles in metallic environments [99].

SUPPLEMENTARY MATERIAL

See the supplementary material for additional figures including ML-MCTDH rate constants at intermediate temperatures, ML-MCTDH flux-side correlation functions, and centroid free energy profiles along the reaction pathways.

ACKNOWLEDGMENTS

Y.L. acknowledges funding from the Deutsche Forschungsgemeinschaft (DFG, German Research Foundation), project number 467724959. P.L. and M.R. thank George Trenins for his valuable discussions and for providing an alternative (more efficient) code for system-bath RPMD. R.M. gratefully acknowledges the INDACO platform, which is a project of High Performance Computing at the Università degli Studi di Milano, for the computational resources allocated at the CINECA HPC center.

DATA AVAILABILITY





The data that support the findings of this study are openly available at https://gitlab.com/litman90/quantum_spatially_varying_friction.

-
- [1] H. Kramers, *Physica* **7**, 284 (1940).
 - [2] P. Hänggi, P. Talkner, and M. Borkovec, *Rev. Mod. Phys.* **62**, 251 (1990).
 - [3] E. Pollak and S. Miret-Artés, *Chem. Phys. Chem.* **24**, e202300272 (2023).
 - [4] U. Weiss, *Quantum Dissipative Systems*, 3rd ed. (World Scientific, 2008).
 - [5] M. Tuckerman, *Statistical Mechanics: Theory and Molecular Simulation* (Oxford University Press, 2010).
 - [6] R. I. Cukier, R. Kapral, and J. R. Mehafeey, *J. Chem. Phys.* **73**, 5254 (2008).
 - [7] F. V. Harald Posch and W. Steele, *Mol. Phys.* **44**, 241 (1981).
 - [8] D. Antoniou and S. D. Schwartz, *J. Chem. Phys.* **110**, 7359 (1999).
 - [9] K. Polley, K. R. Wilson, and D. T. Limmer, *J. Phys. Chem. B* **128**, 4148 (2024).
 - [10] W. Dou and J. E. Subotnik, *J. Chem. Phys.* **148**, 230901 (2018).
 - [11] R. Martinazzo and I. Burghardt, *Phys. Rev. A* **105**, 052215 (2022).
 - [12] R. Martinazzo and I. Burghardt, *Phys. Rev. Lett.* **128**, 206002 (2022).
 - [13] R. Martinazzo and I. Burghardt, arXiv:2310.08766 (2023).

- [14] W. Dou and J. E. Subotnik, *J. Chem. Phys.* **144**, 024116 (2016).
- [15] P. Spiering, K. Shakouri, J. Behler, G.-J. Kroes, and J. Meyer, *J. Phys. Chem. Lett.* **10**, 2957 (2019).
- [16] R. J. Maurer, B. Jiang, H. Guo, and J. C. Tully, *Phys. Rev. Lett.* **118**, 256001 (2017).
- [17] B. Carmeli and A. Nitzan, *Chem. Phys. Lett.* **102**, 517 (1983).
- [18] J. B. Straus, J. M. Gomez Llorente, and G. A. Voth, *J. Chem. Phys.* **98**, 4082 (1993).
- [19] E. B. Brown, *J. Chem. Phys.* **102**, 2288 (1995).
- [20] G. A. Voth, *J. Chem. Phys.* **97**, 5908 (1992).
- [21] R. Krishnan, S. Singh, and G. W. Robinson, *J. Chem. Phys.* **97**, 5516 (1992).
- [22] G. R. Haynes, G. A. Voth, and E. Pollak, *Chem. Phys. Lett.* **207**, 309 (1993).
- [23] G. R. Haynes, G. A. Voth, and E. Pollak, *J. Chem. Phys.* **101**, 7811 (1994).
- [24] G. R. Haynes and G. A. Voth, *J. Chem. Phys.* **103**, 10176 (1995).
- [25] P. G. Wolynes, *Phys. Rev. Lett.* **47**, 968 (1981).
- [26] K. M. Forsythe and N. Makri, *J. Chem. Phys.* **108**, 6819 (1998).
- [27] H. Wang, D. E. Skinner, and M. Thoss, *J. Chem. Phys.* **125**, 174502 (2006).
- [28] I. R. Craig, M. Thoss, and H. Wang, *J. Chem. Phys.* **127**, 144503 (2007).
- [29] I. Navrotskaya and E. Geva, *Chem. Phys.* **322**, 223 (2006).
- [30] Y. Litman, E. S. Pócs, C. L. Box, R. Martinazzo, R. J. Maurer, and M. Rossi, *J. Chem. Phys.* **156**, 194107 (2022).
- [31] T. Yamamoto, *J. Chem. Phys.* **33**, 281 (1960).
- [32] W. H. Miller, S. D. Schwartz, and J. W. Tromp, *J. Chem. Phys.* **79**, 4889 (1983).
- [33] W. H. Miller, *J. Phys. Chem. A* **102**, 793 (1998).
- [34] D. Chandler, *J. Chem. Phys.* **68**, 2959 (2008).
- [35] A. N. Drozdov and S. C. Tucker, *J. Chem. Phys.* **115**, 9675 (2001).
- [36] H.-D. Meyer, U. Manthe, and L. S. Cederbaum, *Chem. Phys. Lett.* **165**, 73 (1990).
- [37] M. H. Beck, A. Jäckle, G. A. Worth, and H.-D. Meyer, *Phys. Rep.* **324**, 1 (2000).
- [38] H.-D. Meyer, F. Gatti, and G. A. Worth, eds., *Multidimensional Quantum Dynamics: MCTDH Theory and Applications* (Wiley-VCH, Weinheim, 2009).
- [39] I. Kondov, M. Čížek, C. Benesch, H. Wang, and M. Thoss, *J. Phys. Chem. C* **111**, 11970 (2007).
- [40] T. Westermann, R. Brodbeck, A. B. Rozhenko, W. Schoeller, and U. Manthe, *J. Chem. Phys.* **135**, 184102 (2011).
- [41] H. Wang, D. E. Skinner, and M. Thoss, *J. Chem. Phys.* **125**, 174502 (2006).
- [42] I. R. Craig and D. E. Manolopoulos, *J. Chem. Phys.* **121**, 3368 (2004).
- [43] S. Habershon, D. E. Manolopoulos, T. E. Markland, and T. F. Miller, *Annu. Rev. Phys. Chem.* **64**, 387 (2013).
- [44] I. R. Craig and D. E. Manolopoulos, *J. Chem. Phys.* **122**, 084106 (2005).
- [45] I. R. Craig and D. E. Manolopoulos, *J. Chem. Phys.* **123**, 034102 (2005).
- [46] T. J. H. Hele and S. C. Althorpe, *J. Chem. Phys.* **139**, 084116 (2013).
- [47] J. O. Richardson and S. C. Althorpe, *J. Chem. Phys.* **131**, 214106 (2009).
- [48] In the asymmetric friction model the system-bath is not symmetric about the barrier, so the optimal dividing surface could potentially mix in non-centroid ring-polymer modes at sufficiently low temperatures.
- [49] M. J. Gillan, *Phys. Rev. Lett.* **58**, 563 (1987).
- [50] G. A. Voth, D. Chandler, and W. H. Miller, *J. Chem. Phys.* **91**, 7749 (1989).
- [51] J. E. Lawrence and D. E. Manolopoulos, *Faraday Discuss.* **221**, 9 (2020).
- [52] R. Collepardo-Guevara, Y. V. Suleimanov, and D. E. Manolopoulos, *J. Chem. Phys.* **130**, 174713 (2009).
- [53] Y. V. Suleimanov, R. Collepardo-Guevara, and D. E. Manolopoulos, *J. Chem. Phys.* **134**, 044131 (2011).
- [54] X. Li and P. Huo, *J. Phys. Chem. Lett.* **12**, 6714 (2021).
- [55] J. W. Allen, W. H. Green, Y. Li, H. Guo, and Y. V. Suleimanov, *J. Chem. Phys.* **138**, 221103 (2013).
- [56] K. M. Hickson, J.-C. Loison, H. Guo, and Y. V. Suleimanov, *J. Phys. Chem. Lett.* **6**, 4194 (2015).
- [57] Y. V. Suleimanov, F. J. Aoiz, and H. Guo, *J. Phys. Chem. A* **120**, 8488 (2016).
- [58] N. Boekelheide, R. Salomon-Ferrer, and T. F. Miller III, *Proc. Nat. Acad. Sci. USA* **108**, 16159 (2011).
- [59] A. Arnaldsson, *Calculation of quantum mechanical rate constants directly from ab initio atomic forces*, Ph.D. thesis, University of Washington (2007).
- [60] W. H. Miller, *J. Chem. Phys.* **62**, 1899 (1975).
- [61] J. O. Richardson, *Int. Rev. Phys. Chem.* **37**, 171 (2018).
- [62] W. Fang, J. O. Richardson, J. Chen, X.-Z. Li, and A. Michaelides, *Phys. Rev. Lett.* **119**, 126001 (2017).
- [63] S. McConnell and J. Kästner, *J. Comput. Chem.* **38**, 2570 (2017).
- [64] J. B. Rommel, T. P. M. Goumans, and J. Kästner, *J. Chem. Theor. Comp.* **7**, 690 (2011).
- [65] J. Nichols, H. Taylor, P. Schmidt, and J. Simons, *J. Chem. Phys.* **92**, 340 (1990).
- [66] Y. Litman, *Tunneling and Zero-Point Energy Effects in Multidimensional Hydrogen Transfer Reactions: From Gas Phase to Adsorption on Metal Surfaces*, Ph.D. thesis, Freie Universität Berlin (2020).
- [67] A. N. Beyer, J. O. Richardson, P. J. Knowles, J. Rommel, and S. C. Althorpe, *J. Phys. Chem. Lett.* **7**, 4374 (2016).
- [68] J. B. Rommel, Y. Liu, H.-J. Werner, and J. Kästner, *J. Phys. Chem. B* **116**, 13682 (2012).
- [69] Y. Litman, J. O. Richardson, T. Kumagai, and M. Rossi, *J. Am. Chem. Soc.* **141**, 2526 (2019).
- [70] Y. Litman and M. Rossi, *Phys. Rev. Lett.* **125**, 216001 (2020).
- [71] W. Fang, J. Chen, P. Pedevilla, X.-Z. Li, J. O. Richardson, and A. Michaelides, *Nat. Comm.* **11**, 1689 (2020).
- [72] M. Topaler and N. Makri, *J. Chem. Phys.* **101**, 7500 (1994).
- [73] A. Caldeira and A. Leggett, *Annals of Physics* **149**, 374 (1983).
- [74] G. A. Worth, M. H. Beck, A. Jäckle, and H.-D. Meyer, The MCTDH Package, Version 8.5. Version 8.2, (2000). H.-D. Meyer, Version 8.3 (2002), Version 8.4 (2007). Current version: 8.4.12 (2016). See <http://mctdh.uni-hd.de>.
- [75] H. Wang, M. Thoss, and W. H. Miller, *J. Chem. Phys.* **115**, 2979 (2001).
- [76] D. Chandler and P. G. Wolynes, *J. Chem. Phys.* **74**, 4078 (1981).

- [77] C. H. Bennett, “Molecular dynamics and transition state theory: The simulation of infrequent events,” in *Algorithms for Chemical Computations* (American Chemical Society, 1977) Chap. 4, pp. 63–97.
- [78] Y. Litman, E. S. Pócs, C. L. Box, R. Martinazzo, R. J. Maurer, and M. Rossi, *J. Chem. Phys.* **156**, 194106 (2022).
- [79] E. Pollak, *Phys. Rev. A* **109**, 022242 (2024).
- [80] L. P. Lindoy, A. Mandal, and D. R. Reichman, *Nat. Commun.* **14**, 2733 (2023).
- [81] H. Grabert, U. Weiss, and P. Hanggi, *Phys. Rev. Lett.* **52**, 2193 (1984).
- [82] S. C. Althorpe, *Eur. Phys. J. B* **94**, 155 (2021).
- [83] R. F. Grote and J. T. Hynes, *J. Chem. Phys.* **73**, 2715 (1980).
- [84] R. F. Grote and J. T. Hynes, *J. Chem. Phys.* **74**, 4465 (1981).
- [85] We assume here that P is odd.
- [86] J. Cao and G. A. Voth, *J. Chem. Phys.* **100**, 5106 (1994).
- [87] E. Pollak, *J. Chem. Phys.* **85**, 865 (1986).
- [88] Note that this equation has to be solved self-consistently.
- [89] P. Hänggi, *Z. Phys. B Condens. Matter* **68**, 181 (1987).
- [90] E. Pollak, H. Grabert, and P. Hänggi, *J. Chem. Phys.* **91**, 4073 (1989).
- [91] Q. Shi, L. Zhu, and L. Chen, *J. Chem. Phys.* **135**, 044505 (2011).
- [92] J. O. Richardson and S. C. Althorpe, *J. Chem. Phys.* **131**, 214106 (2009).
- [93] J. Liu and W. H. Miller, *J. Chem. Phys.* **131**, 074113 (2009).
- [94] J.-L. Liao and E. Pollak, *J. Chem. Phys.* **116**, 2718 (2002).
- [95] Y. Tanimura, *J. Chem. Phys.* **153**, 020901 (2020).
- [96] L. Chen and Q. Shi, *J. Chem. Phys.* **130**, 134505 (2009).
- [97] M. R. Fiechter, J. E. Runeson, J. E. Lawrence, and J. O. Richardson, *J. Phys. Chem. Lett.* **14**, 8261 (2023).
- [98] A. Mandal, M. A. Taylor, B. M. Weight, E. R. Koessler, X. Li, and P. Huo, *Chem. Rev.* **123**, 9786 (2023).
- [99] R.-H. Bi and W. Dou, *J. Chem. Phys.* **160**, 074110 (2024).

Supporting Information: Quantum rates in dissipative systems with spatially varying friction

Oliver Bridge ¹, Paolo Lazzaroni,² Rocco Martinazzo ³,
Mariana Rossi ², Stuart C. Althorpe,¹ and Yair Litman ^{1,*}

¹Yusuf Hamied Department of Chemistry, University of Cambridge, Lensfield Road, Cambridge, CB2 1EW, UK

²MPI for the Structure and Dynamics of Matter, Luruper Chaussee 149, 22761 Hamburg, Germany

³Department of Chemistry, Università degli Studi di Milano, Via Golgi 19, 20133 Milano, Italy

ADDITIONAL FIGURES

In Fig. S1, we compare the transmission factor reported in this work for the uniform friction model at 300K with the results previously reported in the literature by Craig, Wang and Thoss (CTW) [1], and Topaler and Makri (TM) [2]. The three datasets are in perfect agreement.

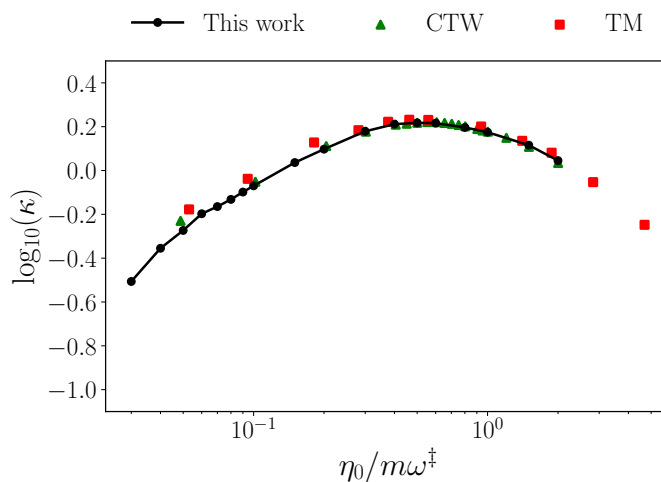


FIG. S1. Comparison of the transmission factors at 300K for the uniform friction model obtained in this work, by Craig, Wang and Thoss (CTW)[1], and by Topaler and Makri (TM)[2].

In Fig. S2, we show the flux-side correlation function obtained with multi-layer multi-configuration time-dependent Hartree (ML-MCTDH) at representative friction values at 300K. In all cases, the coherent tunnelling-dominated regime at low friction can be identified by the presence of oscillation that extends over hundreds of femtoseconds.

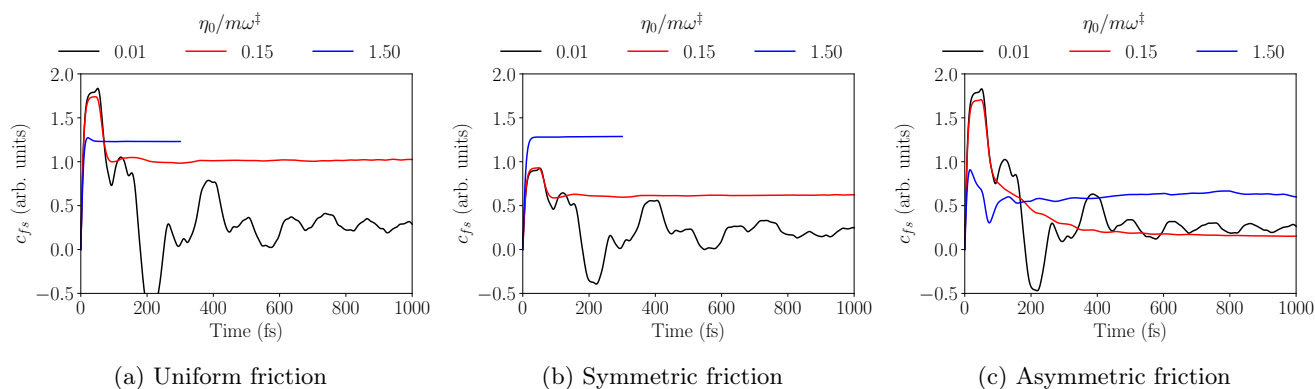


FIG. S2. Flux-side correlation function, $c_{fs}(t)$, obtained with ML-MCTDH at 300K for selected friction values.

In Fig. S3, we report the transmission factors obtained with ML-MCTDH simulations across a wide range of temperatures.

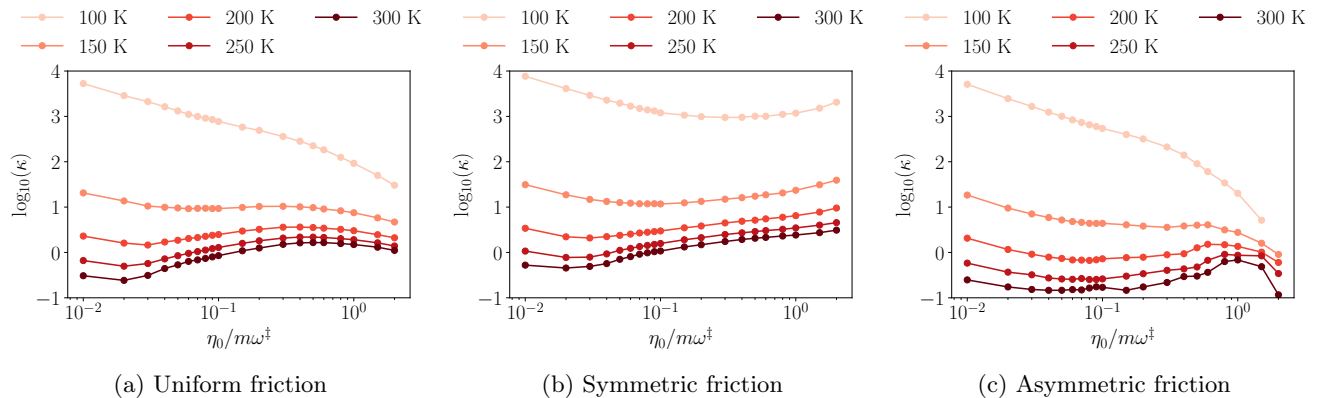


FIG. S3. Transmission factors (Eq. 24 in the main text) obtained from the ML-MCTDH simulations.

Fig. S4 shows the flux-side correlation function, $c_{fs}(t)$, for the uniform model at 300 K over an extended period of time (up to 2250 fs), where the artefacts induced by the bath recurrences can be observed. To increase the bath recurrence time, the development and optimization of a new ML-MCTDH tree structure with a larger number of bath modes would be required.

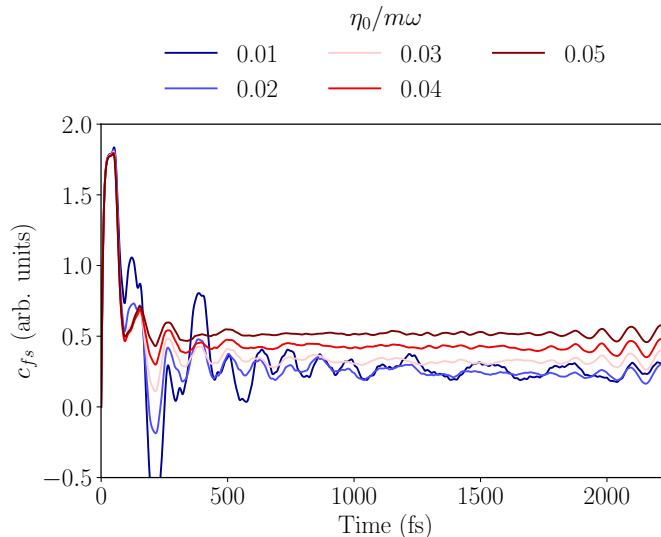


FIG. S4. Extended flux-side correlation function, $c_{fs}(t)$, obtained with ML-MCTDH at 300K for the uniform model. The oscillations that build close to 2000 fs are attributed to bath recurrences.

In Fig. S5, we report the flux-side correlation functions calculated at 200 K for the three models considered. It can be observed that the long-time limit value of $c_{fs}(t)$, which is proportional to the rate constant in this narrow range of friction values, reaches its maximum for the lowest values of friction.

In Fig. S6, we present centroid-free energies along the reaction pathway at 50 K. In the calculations of the uniform model, the free energy in the vicinity of the barrier top flattens out for the lowest friction values, an indication of the ring-polymer delocalization [3, 4], whereas it remains fairly parabolic for the largest values of friction. This qualitative change can be traced back to the appearance of instanton-like geometries at lower friction strengths. Since the crossover temperatures are 71 K and 53 K for $\eta_0/m\omega^\ddagger = 0.3$ and $\eta_0/m\omega^\ddagger = 3.0$, respectively, at 50 K the system is only in the deep-tunneling regime for the former case. In the symmetric model calculations, the changes of the free energy profiles with friction are milder since the instanton geometry expands across areas of relatively small friction. Similar to what is observed at high temperatures, the results of the asymmetric model resemble the uniform case.

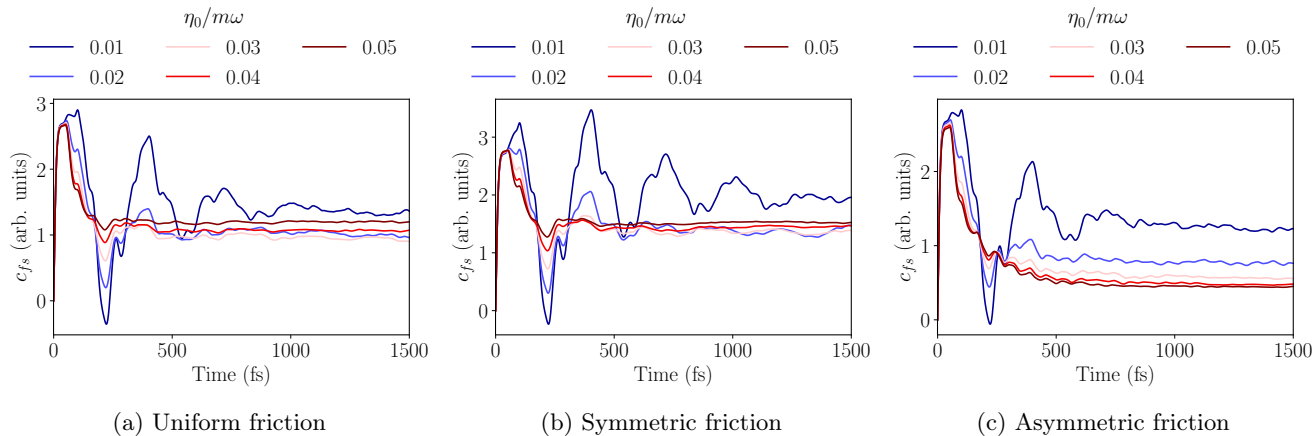


FIG. S5. Flux-side correlation function, $c_{fs}(t)$, obtained with ML-MCTDH at 200K for selected friction values. In all cases, the largest long-time limit value is obtained for the lowest values of friction

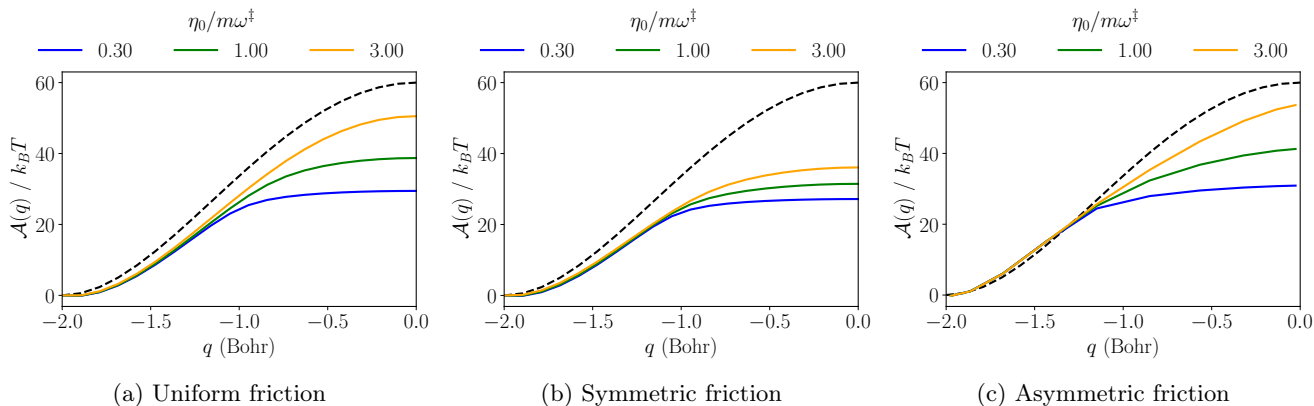


FIG. S6. Centroid free energy along the reaction pathway at 50K for $\eta_0/m\omega_b=0.3$ (blue), $\eta_0/m\omega_b=1.0$ (green), and $\eta_0/m\omega_b=3.0$ (orange). The classical free energy is depicted by a black dashed line.

* Email: yl899@cam.ac.uk

- [1] I. R. Craig, M. Thoss, and H. Wang, *J. Chem. Phys.* **127**, 144503 (2007).
- [2] M. Topaler and N. Makri, *J. Chem. Phys.* **101**, 7500 (1994).
- [3] C. Drechsel-Grau and D. Marx, *Angew. Chem. Int. Ed.* **53**, 10937 (2014).
- [4] J. R. Cendagorta, A. Powers, T. J. H. Hele, O. Marsalek, Z. Bačić, and M. E. Tuckerman, *Phys. Chem. Chem. Phys.* **18**, 32169 (2016).